Ru-Based Catalysts Deposited by Atomic Layer Deposition for Non-Alkaline Zn-Air Batteries

Amit Ohayon,[a, b] Olga Girshevitz,[b] Michal Ejgenberg,[a, b] Gal Radovsky,[b] Malachi Noked,[a, b] and Roman R. Kapaev*[a, b]

Rechargeable zinc-air batteries (ZAB) are a promising energy storage solution due to their low cost, low toxicity and high theoretical energy density. However, conventional alkaline ZABs face challenges such as CO_2 absorption, zinc corrosion, and poor cycle stability. To address these issues, non-alkaline near-neutral electrolytes offer potential benefits, but they also present slower kinetics, especially during the oxygen evolution reaction (OER) at the cell charge. This study investigates the use of atomic layer deposition (ALD) to introduce Ru-based Nano-sites onto carbon cathodes to enhance catalytic activity in non-alkaline ZABs. The catalytic performance of these ALD-treated materials was evaluated in ZABs with 1 M $Zn(OAc)_2$ and 1 M $ZnSO_4$ electrolytes. ALD-treated Ru catalysts significantly lower the OER overpotentials, improving charging capacity and stability of the battery compared to pristine carbon and benchmark RuO_2/C samples with a similar content of ruthenium. We also find that with the Ru-based catalyst, OER proceeds exclusively through the four-electron pathway, in contrast to a mixture of two- and four-electron mechanisms observed for the pristine carbon. Our findings show, using a model catalytical system, that non-alkaline based ZABs can be realized through cathode engineering, and that the reaction mechanism on the cathode is highly dependent on its catalytic properties.

1. Introduction

The growing demand for energy and the shift towards clean and renewable sources has increased the need for advanced energy storage systems. Rechargeable metal-air batteries have gained great interest for energy storage and electric vehicles due to their relatively low cost and high theoretical energy density compared to commonly used Li-ion batteries.[1,2] Among metal-air batteries, zinc-air batteries (ZABs) present a cost-effective, safe, and non-toxic option.[3,4] However, most research in this field has focused on alkaline systems, typically using 6 M KOH as the electrolyte.[3,5,6] Alkaline ZABs suffer from irreversible CO_2 absorption, zinc corrosion, uneven zinc metal growth and cathode degradation.[7,8] These issues limit the potential applications of ZABs as an effective energy storage solution. Alternating to near-neutral electrolytes can potentially address these issues. Non-alkaline electrolytes enable better reversibility

[a] A. Ohayon, M. Ejgenberg, M. Noked, R. R. Kapaev
Department of Chemistry,
Bar-Ilan University,
Ramat-Gan 5290002, Israel
E-mail: kapaevr@biu.ac.il
        kapaev.roman@gmail.com

[b] A. Ohayon, O. Girshevitz, M. Ejgenberg, G. Radovsky, M. Noked, R. R. Kapaev
BIU Center for Nanotechnology and Advanced Materials,
Bar-Ilan University,
Ramat-Gan 5290002, Israel

of zinc electrodeposition, more uniform plating of zinc, and the prevention of irreversible CO_2 consumption.[9,10] However, ZABs with near-neutral electrolytes have been rarely studied. One of the biggest challenges for non-alkaline ZABs is the slow kinetics during battery charging and discharging, particularly during the oxygen evolution reaction (OER) in the charging process, which exhibits high overpotentials.[7,11] A possible solution to this problem is the use of catalysts to improve the kinetics and increase the energy efficiency.[8,12–15] Ru-based catalysts are known as one of the most effective catalysts for OER.[13–16] Common methods for incorporating Ru include wet synthesis, which involves multiple reagents and solvents that can potentially introduce impurities and damage the supporting material.[20,21] In contrast, atomic layer deposition (ALD) is a dry method, offering a cleaner and more efficient approach for Ru deposition.[22,23] In this work, we employ the ALD method to deposit Ru-based catalytically active sites onto carbon scaffold. The deposited Ru nano-sites on the carbon scaffold are used as a model system to evaluate the impact of catalyst on the performance of non-alkaline ZABs, with a particular focus on OER. We show that not only that the catalyst is reducing the overpotential and improves OER kinetics, but it also influences the reaction mechanism in some of the electrolyte solutions.

2. Results and Discussion

2.1. Synthesis and Characterization

To deposit Ru-based catalytic sites on carbon support, we employed the atomic layer deposition (ALD) method, alternating between $Ru(EtCp)_2$ and ozone as precursors for 50, 100, 200, and 500 cycles (Figure 1, see details in Experimental section).
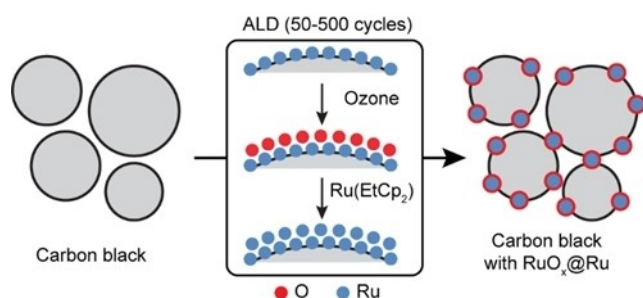
Figure 1. Schematic of the Ruthenium ALD process.

Here and below, these samples are denoted as C—Ru-50, C—Ru-100, C—Ru-200 and C—Ru-500, respectively.

Energy-dispersive X-ray spectra (EDX, Figure 2a) of the samples after ALD contain peaks at 2.5 and 19.3 keV, corresponding to Ru $L_{\alpha1}$ and Ru $K_{\alpha1}$, respectively.[24] The 7.8 and 9.1 keV peaks observed in all samples correspond to copper from the measurement grid.[25] As shown in Figure 2b, X-ray photoelectron spectra (XPS) for C—Ru-200 and C—Ru-500 display two peaks at ~464 eV and ~485 eV, which are attributed to Ru 3p.[26] These peaks are absent for the pristine carbon sample, as well as for C—Ru-50 and C—Ru-100 (Figure S2), due to the Ru content being too low to detect. While the XPS data clearly indicates the presence of Ru in the samples after 200 and 500 cycles, the high noise level and the close proximity of peaks corresponding to different oxidation states[23,24] make it difficult to precisely determine the oxidation state of the Ru sites. Particle Induced X-Ray Emission (PIXE) reveals an expected
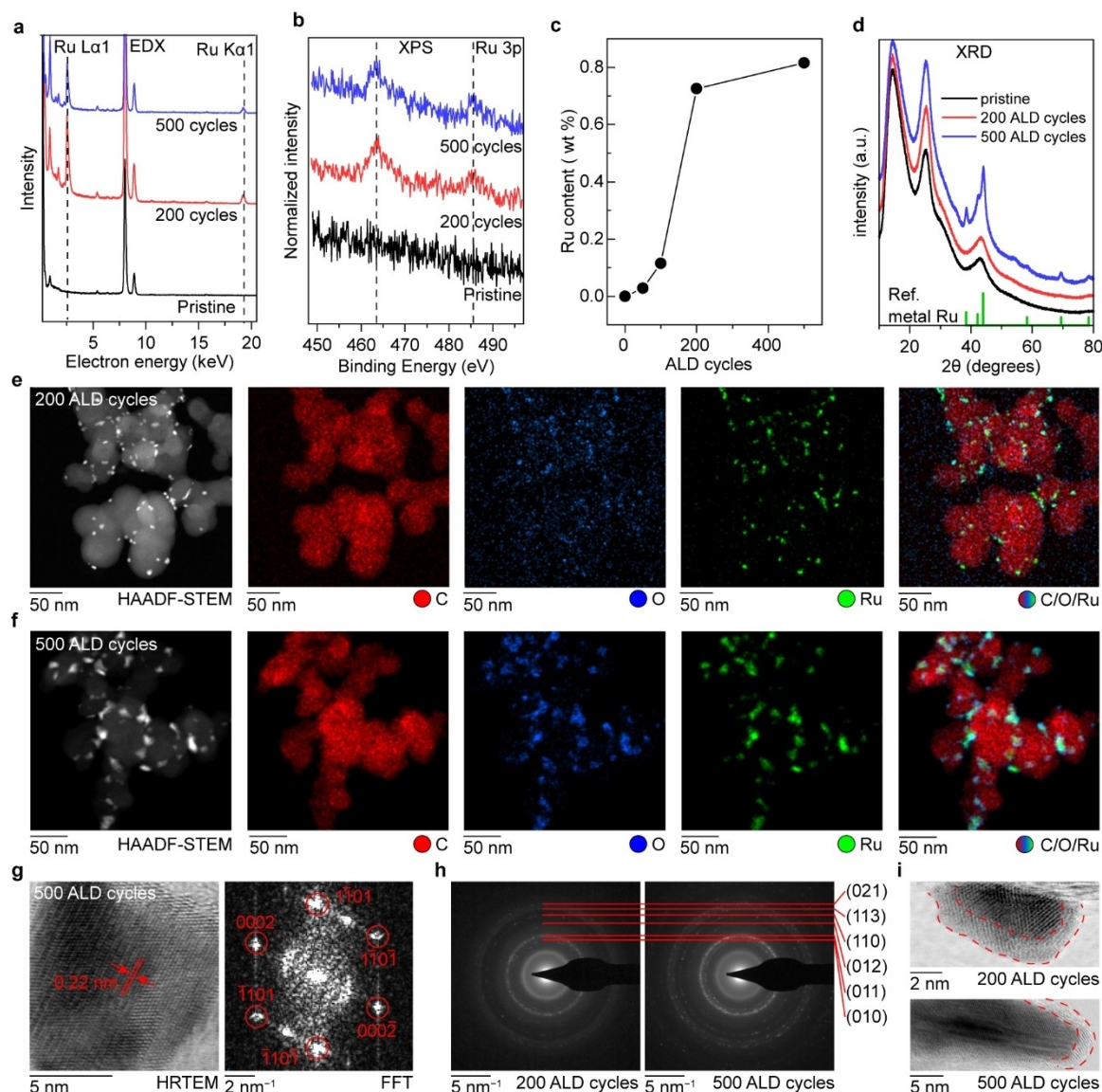

Figure 2. Characterization of carbon black before and after ALD treatment: (a) EDX spectra; (b) Ru 3p XPS; (c) Ru content according to PIXE data; (d) XRD patterns with metal Ru reference (PDF 00-006-0663). HAADF-STEM images and EDX mappings of (e) C—Ru-200 and (f) C—Ru-500. (g) HRTEM image of C—Ru-500 before and after fast Fourier transform (FFT), with 0.22 nm corresponding to (002) plane of Ru metal and characteristic spots of Ru highlighted in the FFT; (h) SAED patterns for C—Ru-200 and C—Ru-500, with characteristic features assigned to planes of Ru metal; (i) HRTEM images of C—Ru-200 and C—Ru-500 revealing the $RuO_x@Ru$ core-shell structure.

Batteries & Supercaps

Research Article
doi.org/10.1002/batt.202400774

Chemistry
Europe

European Chemical
Societies Publishing

increase of Ru content upon increasing the number of ALD cycles (Figure 2d). Initially, there is a delay in the formation of the active sites, this delay has been observed in previous work on Ru ALD and may be attributed to the time required for the precursor molecules to establish nucleation sites on the carbon surface.[20,23,24] The rate of deposition becomes optimal between 100 and 200 cycles. However, after approximately 200 cycles, a slowdown in the deposition rate is observed. This is also common with substrates with non-uniform surface defects that are covered after nucleation and once covered, the rate of growth is dependent on the new surface rather than on defects presence. In any case, the goal of the current work was to fabricate a model scaffold for ORR/OER decorated with catalyst. The mechanism behind the ALD growth of the catalyst is not our main focus.

High-angle annular dark-field scanning transmission electron microscopy images (HAADF-STEM, Figure 2e,f) reveal the presence of well-distributed ~5–15 nm particles in C–Ru-200 and C–Ru-500 samples which are absent in the pristine sample (Figure S1). EDX mapping confirms that these particles contain both ruthenium and oxygen, meaning that they can be represented by RuO_x formula. At the same time, X-ray diffraction (XRD) indicates that C–Ru-500 contains hexagonal metallic Ru.[31] Furthermore, presence of metallic ruthenium is confirmed by high-resolution transmission electron microscopy (HRTEM, Figure 2g) and selected area electron diffraction (SAED, Figure 2h) for C–Ru-200 and C–Ru-500.[32] Elemental ruthenium is a typical product of Ru-based ALD reactions.[33–35] The discrepancy between the EDX mapping and diffraction data might be explained if a core-shell structure $RuO_x@Ru$ is suggested, where Ru metal is covered by amorphous RuO_x. Indeed, such core-shell structures are observed in HRTEM for both C–Ru-200 and C–Ru-500 (Figure 2i). Ruthenium metal cores are crystalline and have higher contrast, while RuO_x shells are poorly ordered and appear brighter because light oxygen element is present. Unfortunately, direct EDX mapping that would reveal different element distribution in the core and shell could not be retrieved for such small particles – RuO_x gets reduced to Ru when exposed to the electron beam for a long time, so sufficiently high signal-to-noise ratio is problematic to obtain for the EDX.

The microscopy images reveal that the $RuO_x@Ru$ particles are smaller for C–Ru-200 (~5–10 nm) than for C–Ru-500 (~10–15 nm). The intensity of Ru features is also weaker in the SAED patterns (Figure 2h). This explains the absence of Ru signals for C–Ru-200 in the XRD pattern (Figure 2d) – the particles are simply too small and give an insufficiently strong signal to be detected by XRD. Overall, the results show an expected trend of particle growth upon increasing the number of ALD cycles.

2.2. Performance in Non-Alkaline Zn-Air Batteries

The catalytic activity of the synthesized materials was evaluated in non-alkaline ZABs with 1 M $Zn(OAc)_2$ or 1 M $ZnSO_4$ as electrolytes (see details in Experimental section). Galvanostatic measurements at a current density of 1 mA cm^{-2} and capacity

of 1 mAh cm^{-2} (Figure 3a, 3b, S4, S5) revealed that the pristine carbon exhibited poor performance in both electrolytes, with lower charging capacity, poor coulombic efficiency and rapid capacity degradation of the cell after only a few cycles. In contrast, the cells with Ru active sites demonstrated significantly better performance, showing equal capacities for both charge and discharge and exhibiting greater stability over time. The observed performance is reproducible (Figure S6), and the difference is attributed to OER reaction kinetics. In the pristine carbon cells, due to the high OER overpotential the cell reaches the cutoff potential of 2.1 V vs. Zn^{2+}/Zn, which is set to prevent corrosion of the stainless-steel current collector.[11] As a result, the charging capacity is significantly reduced. With 1 M $ZnSO_4$ electrolyte, a small plateau is observed around ~1.6 V vs. Zn^{2+}/Zn, which will be discussed in section 2.3. When Ru-based active sites are added, the OER potentials lower to ~1.9 V vs. Zn^{2+}/Zn, allowing the reaction to occur before reaching the cutoff potential. To further investigate OER kinetics, cyclic voltammetry (CV) measurements were performed. The onset voltage of the OER was estimated from the resulting graphs (Figure 3c, 3d, S7). With both 1 M $ZnSO_4$ and 1 M $Zn(OAc)_2$ electrolytes the onset OER potential generally decreased with increasing the Ru content. Additionally, the current increased with increased number of ALD cycles, reflecting improved catalytic activity.
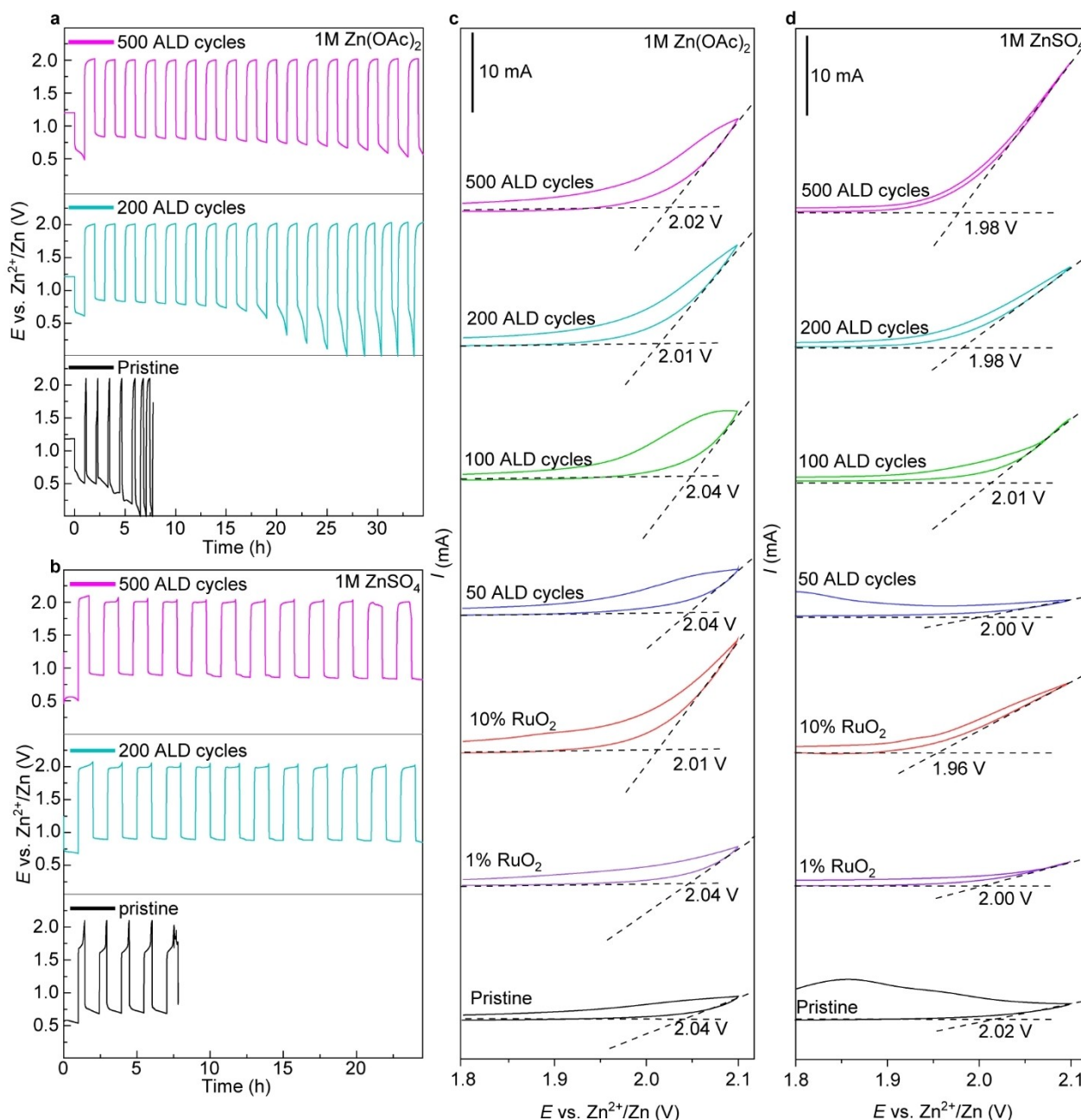
To evaluate the effectiveness of the ALD synthesis, we compared the ALD-synthesized materials with carbon mixed with 1% and 10% wt. RuO_2 nanopowder (Figure 3c, 3d). C–Ru-200 and C–Ru-500 exhibited significantly better performance than cells with 1% RuO_2, with lower onset potentials and improved stability (Figure S4), despite having a similar Ru content. The performance of the cell with 10% wt. nanosized RuO_2 was similar to that of the cells with C–Ru-200 and C–Ru-500, with similar onset potentials in both electrolytes, despite the RuO_2 content being higher by an order of magnitude (10% vs. 0.725% and 0.816% for C–Ru-200 and C–Ru-500, respectively). These findings suggest that the ALD synthesis increases catalytic activity per Ru mass unit. We attribute this to the small size and uniform distribution of $RuO_x@Ru$ particles at the carbon support, which improves availability of the surface sites for catalytic reactions.

2.3. Charge Storage Mechanism

As previously mentioned, in the $ZnSO_4$ electrolyte, a plateau at 1.6 V is observed in the galvanostatic charge of pristine carbon cells (Figure 3b) along with additional anodic peak in the CV (Figure 3d) but this anodic process is absent in the cells with Ru active sites. These different electrochemical behaviors suggest that a different reaction mechanism is occurring. In recent study, we have shown that this plateau is associated with the oxidation of hydrogen peroxide formed during discharge via a two-electron process.[36]

To further explore this, Raman spectra of the electrolytes were measured quickly after the cells were discharged (Figure 4a). Electrolyte from the cell with pristine carbon exhibits a

Batteries & Supercaps

Research Article
doi.org/10.1002/batt.202400774

Chemistry Europe
European Chemical
Societies Publishing

Figure 3. Electrochemical performance of pristine vs. Ru-coated carbon black in non-alkaline Zn-air batteries: galvanostatic cycling at 1 mA cm^{-2} with (a) 1 M Zn(OAc)$_2$ and (b) 1 M ZnSO$_4$ electrolytes; cyclic voltammograms with (c) 1 M Zn(OAc)$_2$ and (d) 1 M ZnSO$_4$.

distinct peak at ~875 cm^{-1}, attributed to the presence of peroxide.[37,38] This peak is absent in the cells with Ru active sites, signifying the absence of peroxide formation and suggesting a different mechanism for ORR and OER. With carbon only, hydrogen peroxide forms during discharge and is subsequently oxidized to water during charging via a two-electron process. Once the peroxide is fully consumed in the 2e-OER, the expected reaction is water oxidation via a four-electron process. However, the overpotential for this reaction is so high that the cell reaches the cutoff voltage before it can occur, leading to a limited charge capacity. When Ru-based sites are added (Figure 4c), no peroxide is detected after

discharge, which explains the absence of the 1.6 V plateau during charging. The sole charging reaction in these cells is the four-electron process, which is catalyzed by the Ru particles and occurs at a much lower potential.

3. Conclusions

In summary, we introduced the importance of heterogenous catalyst in promoting the OER in near-neutral electrolytes for ZAB. To do so, we used a model system of Ru-based catalytic active sites decorated onto a carbon support via ALD method
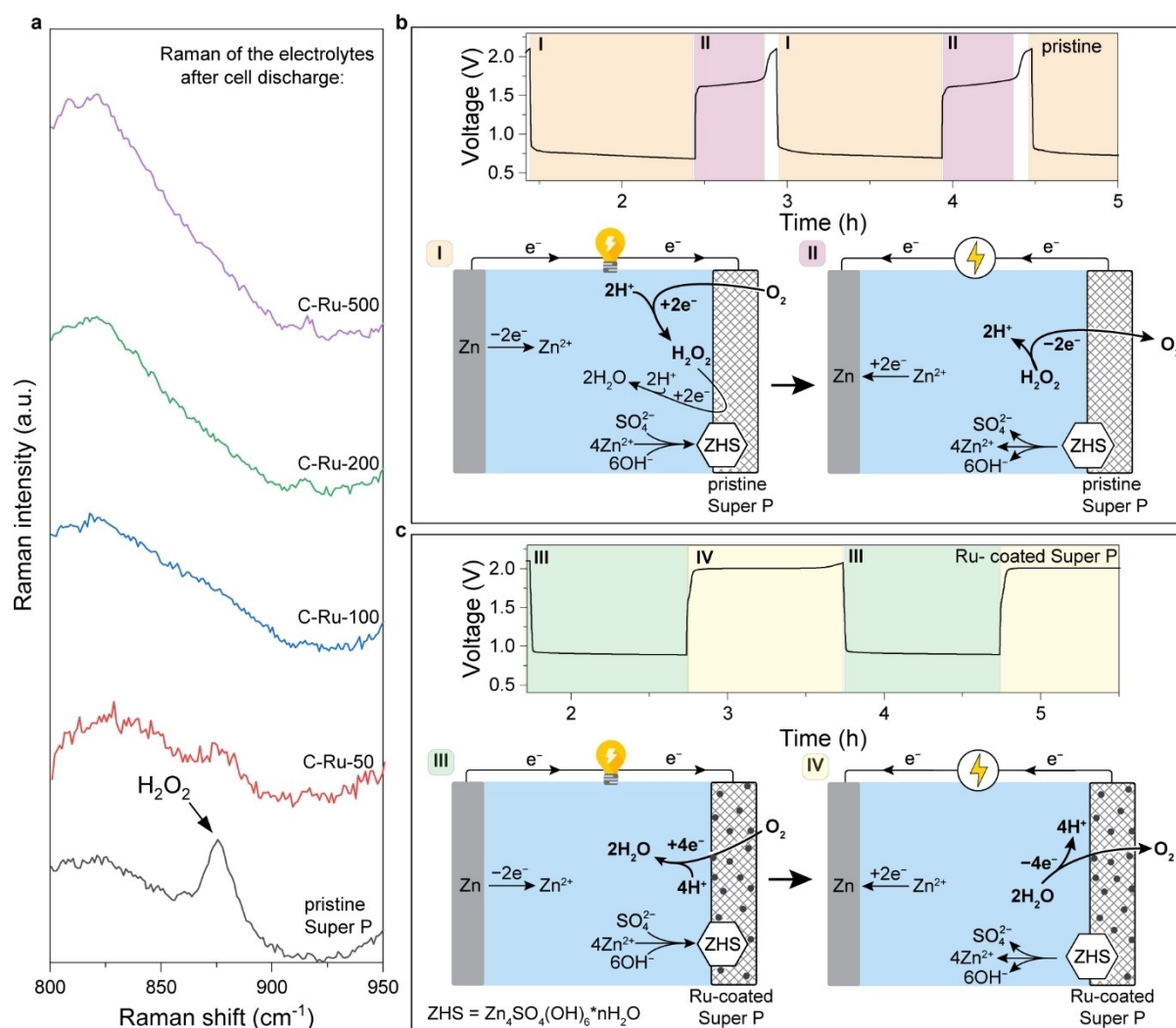
Figure 4. (a) Raman spectra of $ZnSO_4$-based electrolytes after discharging and quickly disassembling the cell with different cathode materials; current-voltage responses at 1 mA cm^{-2} and reaction schemes with 1 M $ZnSO_4$ as electrolyte for (b) pristine carbon and (c) Ru-coated carbon.

using Ru(EtCp)$_2$ and ozone as precursors. This effectively enhanced the performance of the cathode for non-alkaline ZABs. The ALD-treated catalysts showed improved charging capacity, greater stability, and lower overpotentials for OER compared to pristine carbon and benchmark RuO$_2$/C samples with similar Ru contents. Ru active sites prevent peroxide formation, leading to an exclusive four-electron OER path. These findings demonstrate the ALD method's superiority in optimizing catalyst performance for energy storage applications.

Experimental

Materials

Super P Timcal was used as the supporting material. Ru(EtCp)$_2$, Zn(OAc)$_2\cdot$2H$_2$O (ACS reagent, $\geq$98%), ZnSO$_4\cdot$7H$_2$O (ACS reagent, $\geq$99.5%) and polytetrafluoroethylene preparation (60% dispersion in H$_2$O) were purchased from Sigma Aldrich. Zn foil ($\geq$99.95%, 80 μm thickness, degreased) was supplied by Grillo. Whatman glass microfiber filters (GF/A grade) were used as a separator. Sigracet

39BB carbon paper was purchased from Fuel Cell Store. Isopropanol (HPLC PLUS Gradient grade) was supplied by CARLO ERBA reagents.

RuO$_x$@Ru Deposition Prosses

RuO$_x$@Ru particles were deposited via atomic layer deposition (ALD) in a vacuum reactor (Ultratech Savannah 200), using bis(ethylcyclopentadienyl)ruthenium(II) (Ru(EtCp)$_2$) as the precursor and ozone (generated by an Ultratech ozone generator) as the oxidizing agent. Ru(EtCp)$_2$ was kept in a stainless-steel ALD bubbler at 130°C, and the chamber temperature was maintained at 270°C throughout the process. Super P powder was maintained in a glass tumbler which rotated at 5 rpm during the process for better distribution of the deposition. The process started with a 0.05 s pulse of ozone followed by an argon purge for 15 s, then a 1 s pulse of Ru(EtCp)$_2$ with an exposure time of 15 s, and a 15 s argon purge. This procedure was repeated for 50, 100, 200, and 500 cycles.

Batteries & Supercaps

Research Article
doi.org/10.1002/batt.202400774

Chemistry
Europe

European Chemical
Societies Publishing

Characterization

Scanning Transmition Electron Microscope (STEM) and Energy-Dispersive X-ray Spectroscopy (EDS) analyses were conducted using an Aberration Prob-Corrected S/TEM Themis Z G3 (TFS) operated at 300 KV and equipped with a Ceta camera, a high-angle annular dark field detector (Fischione Instruments), DF/BF detectors and a Super-X EDS detection system (TFS). Additional High resolution transmission electron microscopy (HR-TEM) images were acquired on a JEOL JEM 2100, based on a thermionic Lab6 emitter. The EDS measurements were performed using a Thermo Fisher Scientific Silicon drift detector (SDD). X-ray photoelectron spectroscopy (XPS) analysis was carried out using a Nexsa spectrometer (England) equipped with a mono-chromated, micro-focused, low power Al Ka X-ray source (photon energy 1486.6 eV). Survey and high-resolution spectra were acquired at pass energy of 200 eV and 50 eV, respectively. Source power was normally 72 W. The binding energies of all the elements were recalibrated by setting the CC/CH component of the C 1s peak at 285 eV. The PIXE measurements were performed with 2.0 MeV H^+, 3 μC. The beam spot size was 1.5 mm. FastSDD-C2 X-ray detector was used to collect all spectra. The samples were mounted to the holder by carbon tape. Raman spectra of the electrolytes from discharged cells were measured using a Horiba LabRAM Soleil Raman microscope with the laser excitation wavelength of 532 nm.

Electrode Preparation

A typical cathode was prepared by mixing 150 mg of active material (pristine/ALD coated Super P) with 300 μL of H_2O and 20 mL of a 60% dispersion in H_2O polytetrafluoroethylene (PTFE) for a total of 15 mg of PTFE. The components were mixed in an agate mortar, then 750 μL of isopropanol was added, and the slurry was additionally mixed. The slurry was tape-cast on the micro-porous side of Sigracet 39BB carbon paper. The electrodes were oven-dried at 100 °C, roll-pressed at room temperature, and cut into 11 mm diameter disks.

Cell Assembly

The electrode was measured in custom-made two-electrode cells (see Figure S8). A cell consisted of a metal Zn anode (14 mm diameter), a glass fiber separator (21 mm diameter), an electrolyte (120 μL of 1 M Zn(OAc)2 or ZnSO4 in H2O), the prepared cathode (11 mm diameter), a stainless-steel mesh current collector, and a spring. The measurement ware conduct under ambient air, and the valves were closed to prevent the evaporation of the electrolyte.

Electrochemical Measurements

The cells were repeatedly discharged and charged in galvanostatic mode using a Neware system. The capacity was set to 1 mAh cm^{-2}, the current density was 1.0 mA cm^{-2}, within a voltage window of 0–2.1 V, before cycling the cell was kept in rest for 5 h. in addition a cyclic voltammetry was measured in a BioLogic MPG instrument from 0.5 to 2.1 V at a scan rate of 5 mV s^{-1}.

Acknowledgements

Conflict of Interests

The authors declare no conflict of interest.

Data Availability Statement

The data that support the findings of this study are available from the corresponding author upon reasonable request.

[1] J. W. Choi, D. Aurbach, *Nat Rev. Mater.* **2016**, *1*, 16013
[2] M. A. Rahman, X. Wang, C. Wen, *J. Electrochem. Soc.* **2013**, *160*, A1759–A1771.
[3] K. W. Leong, Y. Wang, M. Ni, W. Pan, S. Luo, D. Y. C. Leung, *Renewable Sustainable Energy Rev.* **2022**, *154*, 111771.
[4] T. Zhou, N. Zhang, C. Wu, Y. Xie, *Energy Environ. Sci.* **2020**, *13*, 1132–1153.
[5] X. X. Wang, X. Yang, H. Liu, T. Han, J. Hu, H. Li, G. Wu, *Small Struct* **2022**, *3*, 2100103.
[6] D. Du, S. Zhao, Z. Zhu, F. Li, J. Chen, *Angew. Chem. Int. Ed.* **2020**, *59*, 18140–18144.
[7] C. Wang, J. Li, Z. Zhou, Y. Pan, Z. Yu, Z. Pei, S. Zhao, L. Wei, Y. Chen, *EnergyChem* **2021**, *3*, 2589–7780, DOI 10.1016/j.enchem.2021.100055
[8] J. Zhang, Q. Zhou, Y. Tang, L. Zhang, Y. Li, *Chem. Sci.* **2019**, *10*, 8924–8929, DOI 10.1039/c9sc04221k.
[9] W. Sun, V. Küpers, F. Wang, P. Bieker, M. Winter, *Angew. Chem. Int. Ed.* **2022**, *61*, e202207353.
[10] S. Zhao, T. Liu, J. Wang, I. Temitope Bello, Y. Zuo, M. Wei, K. Wang, K. K. S. Lau, M. Ni, *Chem. Eng. J.* **2022**, *450*, 138207.
[11] R. R. Kapaev, A. Ohayon, M. Sonoo, J. Tzadikov, M. Shalom, M. Noked, *Electrochim. Acta* **2023**, *456*, 142462.
[12] F. Cheng, J. Chen, *Chem. Soc. Rev.* **2012**, *41*, 2172–2192.
[13] Z. Bi, H. Zhang, X. Zhao, Y. Wang, F. Tan, S. Chen, L. Feng, Y. Zhou, X. Ma, Z. Su, X. Wang, T. Wågberg, G. Hu, *Energy Storage Mater.* **2023**, *54*, 313–322.
[14] Z. Nie, M. Chen, L. Zhang, Q. Feng, J. Hu, X. Huang, C. Zhou, Y. Zhou, T. Wågberg, G. Hu, *Chem. Eng. J.* **2023**, *463*, 142411.
[15] X. Zhao, J. Chen, Z. Bi, S. Chen, L. Feng, X. Zhou, H. Zhang, Y. Zhou, T. Wågberg, G. Hu, *Adv. Sci.* **2023**, *10*, 2205889.
[16] J. Ying, J. B. Chen, Y. X. Xiao, S. I. Cordoba de Torresi, K. I. Ozoemena, X. Y. Yang, *J Mater Chem A Mater* **2023**, *11*, 1634–1650.
[17] R. R. Rao, M. J. Kolb, N. B. Halck, A. F. Pedersen, A. Mehta, H. You, K. A. Stoerzinger, Z. Feng, H. A. Hansen, H. Zhou, L. Giordano, J. Rossmeisl, T. Vegge, I. Chorkendorff, I. E. L. Stephens, Y. Shao-Horn, *Energy Environ. Sci.* **2017**, *10*, 2626–2637.
[18] J. Yu, Q. He, G. Yang, W. Zhou, Z. Shao, M. Ni, *ACS Catal.* **2019**, *9*, 9973–10011.
[19] R. Forgie, G. Bugosh, K. C. Neyerlin, Z. Liu, P. Strasser, *Electrochem. Solid-State Lett.* **2010**, *13*, B36.
[20] C. Xu, M. Ming, Q. Wang, C. Yang, G. Fan, Y. Wang, D. Gao, J. Bi, Y. Zhang, *J Mater Chem A Mater* **2018**, *6*, 14380–14386.
[21] J. Kang, S. Zhang, Q. Zhang, Y. Wang, *Angew. Chem. Int. Ed.* **2009**, *48*, 2565–2568.
[22] J. R. Bakke, K. L. Pickrahn, T. P. Brennan, S. F. Bent, *Nanoscale* **2011**, *3*, 3482–3508.
[23] J.-Y. Kim, D.-S. Kil, J.-H. Kim, S.-H. Kwon, J.-H. Ahn, J.-S. Roh, S.-K. Park, *J. Electrochem. Soc.* **2012**, *159*, H560–H564.
[24] Z. B. Wang, G. P. Yin, J. Zhang, Y. C. Sun, P. F. Shi, *J. Power Sources* **2006**, *160*, 37–43.
[25] N. Ahmed, R. Ahmed, M. Rafiqe, M. A. Baig, *Laser Part. Beams* **2017**, *35*, 1–9.
[26] J. Wang, Q. Yu, H. Li, R. Li, S. Zeng, Q. Yao, Z. Guo, H. Chen, K. Qu, *Chem. Commun.* **2021**, *57*, 7284–7287.
[27] M. A. Ernst, W. G. Sloof, *Surf. Interface Anal.* **2008**, *40*, 334–337.
[28] Y. Kaga, Y. Abe, H. Yanagisawa, M. Kawamura, K. Sasaki, *Surf. Sci. Spectra* **1999**, *6*, 68–74.

[29] J. H. Kim, D. S. Kil, S. J. Yeom, J. S. Roh, N. J. Kwak, J. W. Kim, *Appl. Phys. Lett.* **2007**, *91*, 052908, DOI 10.1063/1.2767769.

[30] E. A. Smirnova, A. V. Miakonkikh, A. E. Rogozhin, K. V. Rudenko, *J Phys Conf Ser* **2020**, *1695*, 012045.

[31] X. Shen, L. J. Garces, Y. Ding, K. Laubernds, R. P. Zerger, M. Aindow, E. J. Neth, S. L. Suib, *Appl Catal A Gen* **2008**, *335*, 187–195.

[32] P. Sivakumar, R. Ishak, V. Tricoli, *Electrochim. Acta* **2005**, *50*, 3312–3319.

[33] I. K. Igumenov, P. P. Semyannikov, S. V. Trubin, N. B. Morozova, N. V. Gelfond, A. V. Mischenko, J. A. Norman, *Surf. Coat. Technol.* **2007**, *201*, 9003–9008.

[34] R. Müller, L. Ghazaryan, P. Schenk, S. Wolleb, V. Beladiya, F. Otto, N. Kaiser, A. Tünnermann, T. Fritz, A. Szeghalmi, *Coating* **2018**, *8*, 413, DOI 10.3390/coatings8110413.

[35] K. Gregorczyk, L. Henn-Lecordier, J. Gatineau, C. Dussarrat, G. Rubloff, *Chem. Mater.* **2011**, *23*, 2650–2656.

[36] R. R. Kapaev, N. Leifer, A. R. Kottaichamy, A. Ohayon, L. Wu, M. Shalom, M. Noked, *Angew. Chem. Int. Ed.* **2024**, e202418792. DOI 10.1002/anie.202418792.

[37] Y. Shiraishi, Y. Ueda, A. Soramoto, S. Hinokuma, T. Hirai, *Nat. Commun.* **2020**, *11*, 1–9.

[38] Z. Li, X. Yu, X. Wu, Y. Qiao, S. Ye, *J. Phys. Chem. C* **2024**, *128*, 17878–17885, DOI 10.1021/ACS.JPCC.4C05865.